

Unveiling localized electronic properties of ReS_2 thin layers at nanoscale using Kelvin force probe microscopy combined with tip-enhanced Raman spectroscopy

Yu Luo(罗宇), Weitao Su(苏伟涛), Juanjuan Zhang(张娟娟), Fei Chen(陈飞), Ke Wu(武可), Yijie Zeng(曾宜杰), and Hongwei Lu(卢红伟)

Citation: Chin. Phys. B, 2023, 32 (**11**): 117801. DOI: 10.1088/1674-1056/ace425
Journal homepage: http://cpb.iphy.ac.cn; http://iopscience.iop.org/cpb

What follows is a list of articles you may be interested in

Multifunctional light-field modulation based on hybrid nonlinear metasurfaces

Shuhang Qian(钱树航), Kai Wang(王凯), Jiaxing Yang(杨加兴), Chao Guan(关超), Hua Long(龙华), and Peixiang Lu(陆培祥)
Chin. Phys. B, 2023, 32 (**10**): 107803. DOI: 10.1088/1674-1056/acdc13

Enhanced photoluminescence of monolayer MoS_2 on stepped gold structure

Yu-Chun Liu(刘玉春), Xin Tan(谭欣), Tian-Ci Shen(沈天赐), and Fu-Xing Gu(谷付星)
Chin. Phys. B, 2022, 31 (**8**): 087803. DOI: 10.1088/1674-1056/ac657b

Effect of surface plasmon coupling with radiating dipole on the polarization characteristics of AlGaN-based light-emitting diodes

Yi Li(李毅), Mei Ge(葛梅), Meiyu Wang(王美玉), Youhua Zhu(朱友华), and Xinglong Guo(郭兴龙)
Chin. Phys. B, 2022, 31 (**7**): 077801. DOI: 10.1088/1674-1056/ac4cbb

Exciton luminescence and many-body effect of monolayer WS_2 at room temperature

Jian-Min Wu(吴建民), Li-Hui Li(黎立辉), Wei-Hao Zheng(郑玮豪), Bi-Yuan Zheng(郑弼元), Zhe-Yuan Xu(徐哲元), Xue-Hong Zhang(张学红), Chen-Guang Zhu(朱晨光), Kun Wu(吴琨), Chi Zhang(张弛), Ying Jiang(蒋英),Xiao-Li Zhu(朱小莉), and Xiu-Juan Zhuang(庄秀娟)
Chin. Phys. B, 2022, 31 (**5**): 057803. DOI: 10.1088/1674-1056/ac380c

Surface-enhanced fluorescence and application study based on Ag-wheat leaves

Hongwen Cao(曹红文), Liting Guo(郭立婷), Zhen Sun(孙祯), Tifeng Jiao(焦体峰), and Mingli Wang(王明利)
Chin. Phys. B, 2022, 31 (**3**): 037803. DOI: 10.1088/1674-1056/ac1f0d

---

Unveiling localized electronic properties of ReS_2 thin layers at nanoscale using Kelvin force probe microscopy combined with tip-enhanced Raman spectroscopy

Yu Luo(罗宇)[1], Weitao Su(苏伟涛)[1,†], Juanjuan Zhang(张娟娟)[2,‡], Fei Chen(陈飞)[3], Ke Wu(武可)[1], Yijie Zeng(曾宜杰)[1], and Hongwei Lu(卢红伟)[1]

[1] *School of Sciences, Hangzhou Dianzi University, Hangzhou* 310018, *China*
[2] *Hunan Petrochemical Vocational Technology College, Yueyang* 414011, *China*
[3] *College of Materials and Environmental Engineering, Hangzhou Dianzi University, Hangzhou* 310018, *China*

(Received 24 April 2023; revised manuscript received 1 July 2023; accepted manuscript online 5 July 2023)

Electronic properties of two-dimensional (2D) materials can be strongly modulated by localized strain. The typical spatial resolution of conventional Kelvin probe force microscopy (KPFM) is usually limited in a few hundreds of nanometers, and it is difficult to characterize localized electronic properties of 2D materials at nanoscales. Herein, tip-enhanced Raman spectroscopy (TERS) is proposed to combine with KPFM to break this restriction. TERS scan is conducted on ReS_2 bubbles deposited on a rough Au thin film to obtain strain distribution by using the Raman peak shift. The localized contact potential difference (CPD) is inversely calculated with a higher spatial resolution by using strain measured by TERS and CPD-strain working curve obtained using conventional KPFM and atomic force microscopy. This method enhances the spatial resolution of CPD measurements and can be potentially used to characterize localized electronic properties of 2D materials.

Keywords: few layer ReS_2, tip enhanced Raman spectroscopy, local strain, Kelvin probe force microscopy

PACS: 78.67.–n, 07.79.Fc, 07.79.Lh **DOI:** 10.1088/1674-1056/ace425

1. Introduction

Two-dimensional (2D) transition metal dichalcogenides (TMDs) have drawn much attention recently owing to their unique layered structures and excellent physical properties.[1–4] Rhenium disulfide (ReS_2) is an important member of these layered TMDs, in terms of its unique anisotropic optical and electronic properties.[5–7] ReS_2 has a distorted 1T structure as its stable phase.[8] In (100) plane, the atoms of a ReS_2 layer exist in the form of strong covalent bonds, while the neighboring layers are stacked by weak van der Waals force along [001] direction.[5] At the same time, the metallic Re–Re bond causes the Re4 atomic cluster to form highly oriented Re–Re chains along the lattice direction of the *b*-axis, [010], forming two rhombic edges with an included angle of 118.97° from the *a*-axis,[9] which lowers the crystal symmetry. Due to such an unique structure, the optical, electrical, and optoelectronic properties of ReS_2 thin layers exhibit significant in-plane and out-of-plane anisotropy.[7,10] Moreover, the band structure of ReS_2 thin layers is independent of the layer thickness, i.e., both single-layer and multi-layer ReS_2 possess direct-band gaps.[9] Compared to other conventional TMDs, ReS_2 provides a wider range for exploring advanced electronic and optoelectronic devices, such as logic inverters with higher amplification gain,[11] higher performance field effect transistors,[12] and high-sensitivity polarized light detection.[13]

For a new generation atomic scale device manufactured using ReS_2 thin layers, hardly removed imperfect structures, such as strain,[14] twin boundaries,[15] domain boundaries,[16] are expected to induce localized energy band structure and electronic properties at nanoscale region neighboring these imperfect structure. Probing localized electronic properties induced by these imperfect structures demands an analytic tool with nanoscale spatial resolution. Based on electrostatic interactions, Kelvin probe force microscopy (KPFM) performs as an useful tool to obtain the surface potential changes.[17,18] In a dual pass scan of conventional KPFM, the surface morphology is obtained in the first scan by employing an conductive atomic force microscopy (AFM) probe working at tapping mode, then the contact potential difference (CPD) is obtained in the second scan by lifting the probe and maintaining it at a settled height.[19] The electrostatic force between the tip and the sample is not simply the interaction between the tip apex and a certain point of the sample, but the averaged interaction with a larger sample area under the probe apex.[20] Therefore, the obtained CPD is the averaged potential of this large area and affected by the lifting height and diameter of tip apex, resulting in a few hundreds of nanometers in spatial resolution for conventional KPFM,[21,22] and it is difficult to characterize nanoscale localized electrical properties.

Tip-enhanced Raman spectroscopy (TERS), which uti-

†Corresponding author. E-mail: suweitao@hdu.edu.cn
‡Corresponding author. E-mail: josephy881006@163.com

© 2023 Chinese Physical Society and IOP Publishing Ltd

lizes the localized surface plasmon resonance (LSPR), lighting rod effect and tip-substrate coupling effect,[23–26] etc., has emerged as a novel tool to investigate localized optical and electronic properties of TMDs.[26–33] Due to the strongly localized electric field at the tip apex, the spatial resolution of TERS can be several nanometers under ambient conditions[28,34] and even sub-nanometer at helium temperature.[34,35] However, to the best of our knowledge, TERS has not been implemented into characterizing physical properties of ReS_2 thin layers so far. In this work, TERS is combined with KPFM to study localized electronic properties of few-layer ReS_2 flakes mechanically exfoliated on rough gold thin films. We obtain the local strain of ReS_2 bubbles using tip-enhanced Raman spectroscopy and then inversely calculate the CPD changes at the nanoscale. This method overcomes low spatial resolution of conventional KPFM and can be used to characterize localized electrical properties of thin-layer TMDs with higher spatial resolution at nanoscale.

2. Experimental details

Few-layer ReS_2 flakes with low density of defects were mechanically exfoliated from a high-quality ReS_2 crystal (Xianfeng Nano) onto gold thin films (40 nm) coated on Si/SiO_2(300 nm) substrates. Optical images of the samples were captured by an optical microscope (Olympus BX53). Far-field Raman and photoluminescence spectra were collected on a Horiba NanoRaman system (LabRAM HR Nano, HORIBA Scientific, France) in top illumination. The 532 nm excitation laser was focused onto the sample via a 100× Olympus objective lens (NA = 0.9). The laser power at the sample surface was controlled below 100 μW to avoid the overheating effect. TERS measurements were conducted using the same HORIBA NanoRaman system. A He–Ne laser (632.8 nm) was focused onto the apex of Au-coated AFM tips ($k = 2.7$ N/m, $f = 60$ kHz, HORIBA Scientific, France) in side-illumination geometry at an angle of 60° using a 100× long working distance (6 mm) objective lens (Mitutoyo, Japan, 0.7 NA). TERS spectra were obtained using 150 and 1800 lines/mm gratings and an electron-multiplying charged-coupled device detector (HORIBA Scientific, France).

KPFM measurements were performed on the scanning probe microscopy (SPM) unit of the same HORIBA NanoRaman system. Au-coated TERS probes were directly used for the AFM and KPFM measurements. KPFM measurements were performed by lifting the AFM probes 10 nm away from the sample surface.

3. Results and discussion

Optical image of a ReS_2 multi-layer flake deposited on a Au thin film is presented in Fig. 1(a). The area with lightest contrast can be tentatively assigned to 1L. The areas with gradually increasing contrast can be tentatively assigned to 2L and 3L. The area with darkest contrast can be assigned to thick layer (tL). AFM topographic and phase images of a marked area in Fig. 1(a) are shown in Fig. 1(b) and Fig. S1 in the supporting information. Due to large surface roughness of the Au thin film, the 1L area is hardly seen in the topographic image, but can be easily found in the phase image (Fig. S1). A height profile across the terrace between 1L and 3L along the arrowed line in Fig. 1(b) is plotted as an inset [Fig. 1(b)]. The thickness difference between 1L and 3L can be determined to be 1.8 nm. The thickness of 3L was determined to be 2.8 nm by using the height line profiles across 3L and tL (Fig. S2), while the thickness of 1L can be determined to be 1 nm, which agree well with the literatures.[10,36] By combining the optical, height and phase images, this ReS_2 flake can be quarantined into areas with different layer thickness shown in Fig. 1(b).

A CPD image of the ReS_2 area corresponding to Fig. 1(b) is presented in Fig. 1(c). The 1L area has highest CPD as 0.31 ± 0.02 V. For 2L, 3L and tL, their CPDs gradually decrease to 0.24 ± 0.01 V, 0.23 ± 0.01 V and 0.22 ± 0.01 V, respectively. The Fermi level (E_f) of 1L, 2L, 3L and tL can be calculated to be 4.59 ± 0.02, 4.66 ± 0.01, 4.68 ± 0.01 and 4.68 ± 0.01 eV, respectively, by using the equation[37]

$$E_f = \Phi_{Au} - e \times \mathrm{CPD}, \tag{1}$$

where Φ_{Au} is the work function of Au tip (4.9 eV). The measured values of ReS_2 thin layers are in good agreement with the theoretical value (4.63 eV) obtained using the DFT calculation.[38]

Zoomed-in topographic and CPD images of a 3L area marked in Fig. 1(c) are shown in Figs. 1(d) and 1(e), respectively. Due to the large particle size (averaged diameter ∼ 70 nm) and high roughness (RMS roughness, RMS = 3.1 nm) of the gold particles, the ReS_2 area also gives large roughness of RMS = 1.9 nm (Fig. S3). This indicates the 3L ReS_2 bends into bubbles in order to follow the roughness of the gold particles. The bubble like feature is much clear at the edge of this ReS_2 flake (Fig. S3). When the ReS_2 thin layer forms a bubble-like structure covering gold particles, biaxial strain is expected to be generated. For a bubble with a height h and a diameter R, the biaxial strain at the crest can be calculated using the equation[39,40]

$$\varepsilon = \delta(\nu)(h/R)^2, \tag{2}$$

where $\delta(\nu)$ is a parameter that only depends on Poisson's ratio ν. For ReS_2 with an average $\nu = 0.225$,[41] $\delta(\nu)$ can be set to be 0.6. The strain distributions of the bubbles are also calculated based on the membrane theory of solid mechanics[42] (Note 1 in the supporting information), which is exemplified in Fig. S4.

In the CPD image shown in Fig. 1(e), the CPD value at the valley of bubbles is hard to be determined due to large noise. Moreover, the low spatial resolution of KPFM scan (49.6 ± 18.9 nm, Fig. S5) also inhibits the accurate imaging of the CPD distribution in the whole ReS_2 bubble area. Luckily the CPDs at crest of some bubbles can still be obtained. The CPDs at crests 14 bubbles (see Figs. S6a and S6b for their locations) were measured and plotted as a function of their strain calculated using Eq. (2), as shown by scatters in Fig. 1(f). The CPD as a function of strain at the crest of bubble calculated based on the membrane theory are also plotted as scatters in Fig. 1(f), which agrees well with the calculated results using Eq. (2) when strain $> 0.2\%$, indicating the validity of the calculations using Eq. (2). These CPDs can be well fitted by a 4th order polynomial function of strain as follows:

$$\mathrm{CPD} = 37.5 - 231\varepsilon + 992\varepsilon^2 - 1597\varepsilon^3 + 920\varepsilon^4. \quad (3)$$

The fitted data is plotted as a solid line in Fig. 1(f). Best fit gives a V-shape curve with the minimum CPD at strain of 0.2%. The trend of the CPD–strain curve in strain $> 0.2\%$ agrees well with that of ReS_2 bubbles reported by Long *et al.*[43] The measured CPD of ReS_2 is inversely proportional to its Fermi level, which has been defined as $E_f = \frac{(E_c+E_v)}{2} + \frac{3k_0T}{4}\ln(m_{dp}/m_{de})$, where E_c (E_v) and m_{dp} (m_{de}) are the energies of conduction band minima (valence band maxima) and effective mass of hole (electron) at the Γ point of the first Brillouin zone.[44] According to the previous reports,[45,46] E_c, E_v, m_{dp} and m_{de} are all dependent on the loaded strain. Detailed quantitative analysis of the V-shape relationship between E_f and strain needs to further consider the in-plane anisotropic electronic properties, which is still ongoing and will be reported in the near future. It should be noted that the relationship of Eq. (3) is obtained by using the strain and CPDs at crests of the bubbles. Because the strain varies from the bottom to the crest of a bubble, the local strain induced CPD variation in the whole area of a bubble cannot be directly obtained by Eq. (3).

ReS_2 belongs to the $P\bar{1}$ group. Bulk ReS_2 has 36 phonon modes including 18 Raman active A_g modes, 15 infrared active A_u modes and 3 acoustic A_u modes.[47] Raman spectra of 1L, 2L, 3L and tL ReS_2 are plotted in Fig. 1(g). Six Raman peaks between 100 cm^{-1} and 250 cm^{-1} can be assigned to A_g modes annotated as A_1 ($\sim$ 137 cm^{-1}), A_2 ($\sim$ 143 cm^{-1}), A_3 (151 cm^{-1}), A_4 (161 cm^{-1}), A_5 (212 cm^{-1}) and A_6 (235 cm^{-1}), of which the peak positions agree well with the reported data.[47,48] Raman peak positions of A_3, A_4 and A_5 modes as a function of layer numbers are plotted in Fig. 1(h). All these three modes redshift for ~ 0.5 cm^{-1} from 1L to tL, which is in agreement with the results reported in the literature[10,49] and can be correlated to the plane bond length contraction and lateral deformation caused by interlayer coupling.[50]

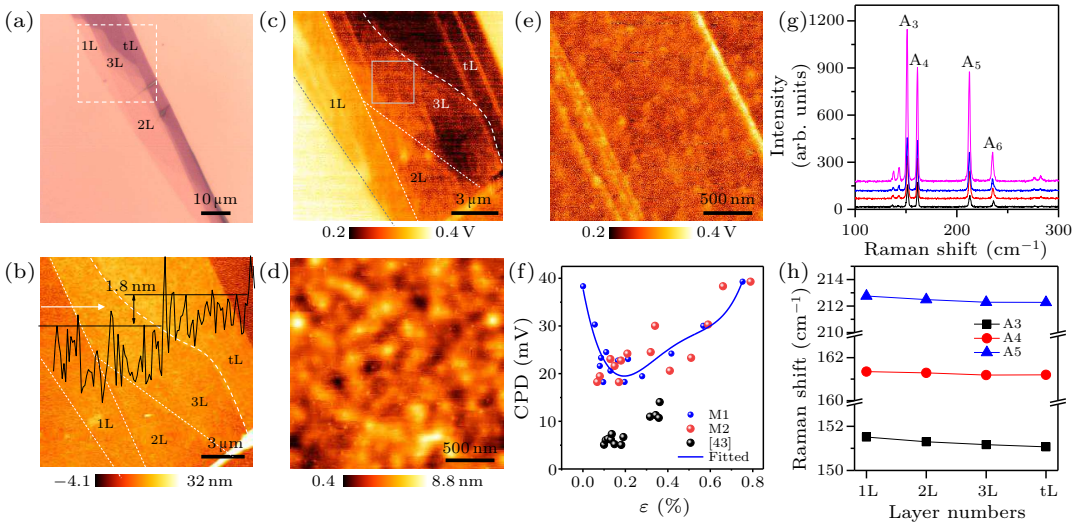


Fig. 1. (a) Optical image of a $ReSe_2$ thin flake; (b) AFM topographic image of the ReS_2 flake in the marked area of (a). Height profile along the marked arrow line is potted as an inset; (c) CPD image corresponding to the area in (b); zoomed-in AFM topographic (d) and CPD (e) images corresponding to the marked area in (c); (f) CPD as a function of strain collected at the top area of different ReS_2 bubbles. M1 refers to the calculation using Eq. (2). M2 refers to the calculation using the membrane theory. The data calculated by M1 are fitted by using a 4th order polynomial function (solid line); (g) Raman spectra of 1L, 2L, 3L and tL, excitation laser wavelength: 532 nm; (h) peak positions of A3, A4 and A5 as a function of layer numbers.

The optical configuration of the TERS setup is shown by a scheme presented in Fig. 2(a). Briefly, a He–Ne laser (632.8 nm) is focused onto the apex of a plasmonic gold coated silicon probe at an angle of 30° via a long working distance lens (see experimental section for details). 1L, 2L and 3L areas were moved to the TERS probe by a piezostage. The obtained tip-in [containing near field (NF) and far field (FF)] and tip-out (FF) Raman spectra are plotted in Fig. 2(b). Because the 150/mm grating gives a spectral resolution of ~ 4 cm^{-1}, fine Raman peaks in Fig. 1(g) cannot be fully scrutinized. The

Raman band B1 at ~ 150 cm^{-1} is predominantly merged by A_3 and A_4 peaks, while band B2 at ~ 220 cm^{-1} was merged by Raman peaks of A_5 and A_6 (see Fig. S7 for the deconvolution of B1 and B2 bands). The TERS spectra of ReS_2 exhibit a layer number and peak dependent enhancement. Single-layer ReS_2 has the strongest enhancement for B1 and B2 bands. The enhancement roughly decreases as the layer number increases from 1L to 3L. However, for thick layer, the enhancement of B1 and B2 becomes slightly larger than that of 3L. The enhancement contrasts of different layers can be calculated by using $C = (I_{\text{tip-in}} - I_{\text{tip-out}})/I_{\text{tip-out}}$,[51] where $I_{\text{tip-in}}$ and $I_{\text{tip-out}}$ are intensities of Raman bands B1 and B2 measured at tip-in and tip-out, respectively. The calculated contrasts of B1 and B2 bands of different layers are plotted as opened circles in Fig. 2(c). For 1L the contrasts of B1 and B2 are calculated to be 0.76 and 0.23, respectively; while for 3L, the contrasts of B1 and B2 decrease to be 0.04 and 0.15, respectively. The enhancement factors are further calculated by using $\text{EF} = C \times D_{\text{focus}}^2/d_{\text{tip}}^2$, where D_{focus} and d_{tip} are diameters of laser focus and TERS spatial resolution,[52] and can be set to be 1000 nm and 10 nm,[30] respectively. In a TERS system operated in gap mode, the TERS intensity decays exponentially with the increasing distance from tip apex to the metallic thin film. As the layer thickness of ReS_2 increases, the gap size is also enlarged, which decreases the enhancement factor.[31] An exponential decay function of enhancement factor, $\text{EF} \propto e^{(d-d_0)/D}$, in which D is a parameter that quantifies the enhanced optical field confinement at the tip apex along the longitudinal direction of the tip axis,[53] is used to fit the enhancement factor of ReS_2 B1 band as a function of layer thickness. Best fitting yields a decay constant D of 0.88 nm, which is very close to the thickness of 1L (Fig. S8).

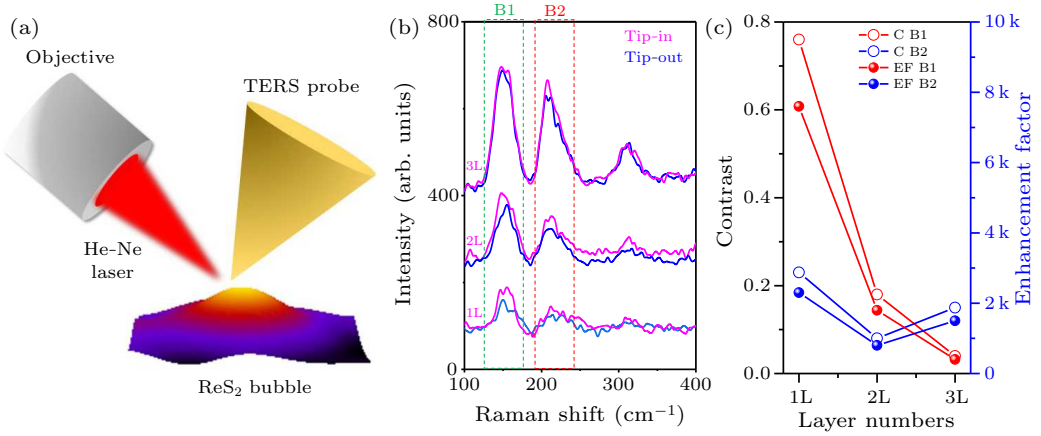


Fig. 2. (a) Scheme of the TERS setup used in this study; (b) tip-in and tip-out Raman spectra of 1L, 2L and 3L $ReSe_2$. The tip-in and tip-out spectra were measured by using a grating of 150 mm^{-1}, which yields the spectrum resolution of ~ 4 cm^{-1} and the A3, A4 and A5 peaks are hardly distinguished. (c) Contrast and enhancement factor of Raman bands B1 and B2 for 1L, 2L and 3L ReS_2.

In further TERS analysis of ReS_2, the strain induced relative peak intensity change and peak shift need to be considered. Li *et al.*[54] calculated the Raman intensity of A_3 and A_4 using the density function theory (DFT) and indicated that their intensity ratio can be enlarged from $I_{A_3}/I_{A_4} < 1$ to > 1 either at tensile or at compressive strain. In the case of strong TERS enhancement like 1L ReS_2, this would not give strong influence. However, in the case of weak TERS enhancement obtained for 3L ReS_2, the local strain induced peak intensity ratio change may be larger than that of enhancement. The unusual stronger enhancement of Raman band B2 than that of B1 shown in Fig. 2(c) is supposed to be induced by this factor.

In TERS analysis of strained ReS_2, peak shift also needs to be considered. In a usual TERS enhancement analysis in which the peak shift is negligible, a pure NF signal is easily obtained by subtracting the FF signal from the NF [see the simulation shown in Figs. 3(a) and 3(b)]. For a local biaxial strain existing on a ReS_2 bubble, Raman peaks A_3 and A_4 are supposed to shift referring to their far-field positions. In the case of weak enhancement, either red shift (RF) or blue shift (BF) of NF signal causes a distorted Raman peak when subtracting the FF from the NF [see the simulation shown in Figs. 3(a) and 3(b)]. The position of the positive peak can still be used as the peak position of the pure NF signals for further calculations, which only gives negligible errors.

The Raman signal of 1L and 2L ReS_2 is much weaker than that of 3L ReS_2 [Fig. 2(b)], indicating that much longer exposure time is needed at each pixel to get useful TERS spectra. Notably, tL ReS_2 has strong Raman signals, whereas the enhancement is much weaker. Therefore, TERS line scan was conducted on 3L so as to balance the TERS enhancement and the exposure time. An AFM topographic image of a 3L ReS_2 area is presented in Fig. 3(c). TERS line scan was conducted in the marked area of Fig. 3(c). The scanned area is 200×20 nm with 20×2 pixels. The obtained TERS spectra are stacked and shown in Fig. 3(d). Compared to the peak position measured at the bottom of the bubble, both Raman peak A3 and A4 redshift by 0.5–1 cm^{-1} at the crest of the bubble. The second line scan (line 2, from pixel 21 to 40) shows similar red shift analogy to the first line scan (line 1, from pixel 1 to

20), indicating the reproducibility of the measurements. In the measured bubble area, no defects or impurities can be seen either in AFM height [Fig. 3(c)] or in CPD images. Therefore, the Raman shift can be attributed to the bubble induced strain rather than impurities or defects. The A_3, A_4 and A_5 peak positions of the scanned pixels are obtained by fitting the subtracted NF spectra using Lorentzian functions and plotted as scatters in Fig. 3(e). These TERS peak positions as a function of positions across the bubble are further fitted by quadratic polynomial functions, as shown by solid lines in Fig. 3(e).

The strain induced Raman peak shift can be expressed as[55–57]

$$\varepsilon = \varepsilon_r + \varepsilon_\theta = (\omega - \omega_0)/(2\gamma\omega_0), \tag{4}$$

where ω_0 is the Raman peak position at zero strain, which was determined from ReS_2 flakes mechanically exfoliated on SiO_2(300 nm)/Si substrates; γ is Grüneisen parameter; ε_r and ε_θ are the strains along radial and circumferential directions, respectively.

The loaded force F leading to the radial and circumferential strains can be expressed as[56]

$$\varepsilon_r = \frac{3-\nu}{4}\left(\frac{F^2}{3\pi^2E^2d^2}\right)^{1/3}\left(\frac{1}{R}\right)^{2/3}, \tag{5}$$

$$\varepsilon_\theta = \frac{1-3\nu}{4}\left(\frac{F^2}{3\pi^2E^2d^2}\right)^{1/3}\left(\frac{1}{R}\right)^{2/3}, \tag{6}$$

where E is Young's modulus, d is the thickness of the flake. With Poisson's ratio $\nu = 0.225$, ε_r is calculated to be 8.6 times larger than ε_θ. Therefore, for a ReS_2 bubble the radial strain is predominant, while the circumferential strain is negligible and can be neglected.

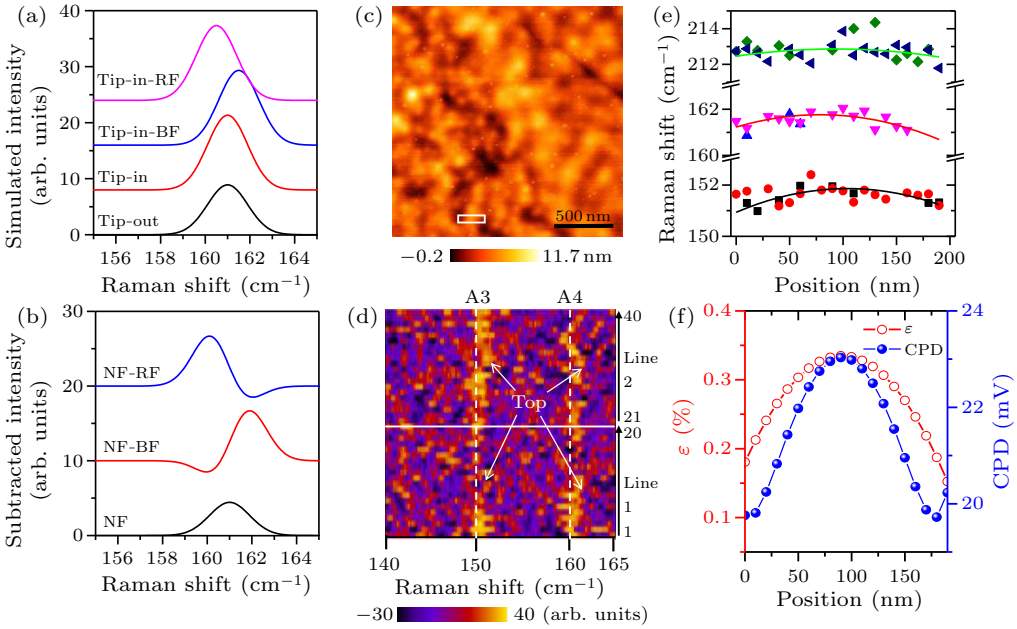


Fig. 3. (a) Simulated tip-in and tip-out and (b) subtracted near-field (NF) Raman spectra collected at crest and bottom of a ReS_2 bubble. BF and RF refer to blue shift and red shift, respectively. In the simulation, a typical peak with width of 1.7 cm^{-1} is used. The typical red and blue shift of 0.5 cm^{-1} is used. (c) AFM topographic image of the TERS scanned area; (d) two TERS line scans along the marked area in (c); (e) TERS peak positions as a function of position across the ReS_2 bubble; (f) calculated strain and CPD versus position across the ReS_2 bubble.

According to the theoretical calculations, the γ values for A_3, A_4, and A_5 peaks are 1.4, 1.3, and 2.8, respectively.[58] The strains at different positions across the ReS_2 bubble can be calculated through Eq. (4) by using Raman peak shifts of A_3, A_4 and A_5. The obtained strains using A_3, A_4 and A_5 peaks are averaged to eliminate the random errors, which are further plotted in Fig. 3(f). The largest tensile strain of 0.34% is seen at the crest of the bubble, while the smallest tensile strain of 0.18% is seen at the bottom of the bubble.

Using this strain distribution curve as the working curve, we calculate the CPD as a function of position by employing Eq. (3), as plotted in Fig. 3(f). It is worth noting that the spatial resolution of CPD calculated using Raman shift is strongly dependent on the pixel size of TERS line scan. The typical spatial resolution of our TERS system is better than 10 nm, indicating that the spatial resolution of this method is also better than 10 nm. Such a spatial resolution is ~ 5 times better than that of the KPFM measurement. The localized electronic properties of other TMDs are expected to be measured at nanoscale by using this method.

4. Conclusions

In summary, we have proposed to characterize localized electronic properties of a ReS_2 thin layer by combining TERS with conventional KPFM measurement. The strain at different positions of a ReS_2 bubble can be obtained from the TERS peak shift by using Grüneisen relationship. The local CPD at

nanoscale is further obtained by using the strain-CPD relationship obtained via conventional KPFM instrument. The spatial resolution of the proposed method only depends on the spatial resolution of TERS and can be potentially improved to be several nanometers, which is $< 1/5$ of that of conventional KPFM measurements. It is worth noting that this method is also applicable to other 2D materials in which local strain is the major factor modulating the localized electronic properties. This method breaks the spatial resolution limitation of conventional KPFM measurement and paves the way of characterizing the localized electronic properties with an alternative optical spectral method.

Acknowledgments

Project supported by the Zhejiang Provincial Natural Science Foundation of China (Grant No. LZ22A040003) and the National Natural Science Foundation of China (Grant No. 52027809).

References

[1] Li X and Zhu H 2015 *J. Materiomics* **1** 33
[2] McDonnell S J and Wallace R M 2016 *Thin Solid Films* **616** 482
[3] Cheng Y, Wei X X, Guo D, Wu B, Yu L W, Wang X R and Shi Yi 2015 *Chin. Phys. Lett.* **32** 117801
[4] Li J H, Bing D, Wu Z T, Wu G Q, Bai J, Du R X and Qi Z Q 2020 *Chin. Phys. B* **29** 017802
[5] Friemelt K, Lux-Steiner M C and Bucher E 1993 *J. Appl. Phys.* **74** 5266
[6] Lin D Y, Huang T P, Wu F L, Lin C M, Huang Y S and Tiong K K 2011 *Solid State Phenomena* **170** 135
[7] Wolverson D, Crampin S, Kazemi A S, Ilie A and Bending S J 2014 *ACS Nano* **8** 11154
[8] Xiong Y, Chen H, Zhang D W and Zhou P 2019 *Physica Status Solidi RRL* **13** 1800658
[9] Tongay S, Sahin H, Ko C, Luce A, Fan W, Liu K, Zhou J, Huang Y S, Ho C H, Yan J, Ogletree D F, Aloni S, Ji J, Li S, Li J, Peeters F M and Wu J 2014 *Nat. Commun.* **5** 3252
[10] Chenet D A, Aslan B, Huang P Y, Fan C, van der Zande A M and Heinz T F and Hone J C 2015 *Nano Lett.* **15** 5667
[11] Liu E, Fu Y, Wang Y, Feng Y, Liu H, Wan X, Zhou W, Wang B, Shao L, Ho C H, Huang Y S, Cao Z, Wang L, Li A, Zeng J, Song F, Wang X, Shi Y, Yuan H, Hwang H Y, Cui Y, Miao F and Xing D 2015 *Nat. Commun.* **6** 6991
[12] Corbet C M, McClellan C, Rai A, Sonde S S, Tutuc E and Banerjee S K 2015 *ACS Nano* **9** 363
[13] Liu F, Zheng S, He X, Chaturvedi A, He J, Chow W L, Mion T R, Wang X, Zhou J, Fu Q, Fan H J, Tay B K, Song L, He R H, Kloc C, Ajayan P M and Liu Z 2016 *Adv. Funct. Mater.* **26** 1169
[14] Fujita T, Ito Y, Tan Y, Yamaguchi H, Hojo D, Hirata A, Voiry D, Chhowalla M and Chen M 2014 *Nanoscale* **6** 12458
[15] Huang L, Zheng F, Chen H, Thi Q H, Chen X, Liu H, Lee C S, Deng Q, Zhao J and Ly T H 2021 *Commun. Mater.* **2** 87
[16] Li X, Wang X, Hong J, Liu D, Feng Q, Lei Z, Liu K, Ding F and Xu H 2019 *Adv. Funct. Mater.* **29** 1906385
[17] Glatzel T, Gysin U and Meyer E 2022 *Microscopy* **71** i165
[18] Loos J 2005 *Adv. Mater.* **17** 1821
[19] Yasutake M, Aoki D and Fujihira M 1996 *Thin Solid Films* **273** 279
[20] Baier R, Leendertz C, Lux-Steiner M C and Sadewasser S 2012 *Phys. Rev. B* **85** 165436
[21] Li F, Qi J, Xu M, Xiao J, Xu Y, Zhang X, Liu S and Zhang Y 2017 *Small* **13** 1603103
[22] Kaushik V, Varandani D and Mehta B R 2015 *J. Phys. Chem. C* **119** 20136
[23] Kumar N, Weckhuysen B M, Wain A J and Pollard A J 2019 *Nat. Protocols* **14** 1169
[24] Richard-Lacroix M, Zhang Y, Dong Z and Deckert V 2017 *Chem. Soc. Rev.* **46** 3922
[25] Pozzi E A, Goubert G, Chiang N, Jiang N, Chapman C T, McAnally M O, Henry A I, Seideman T, Schatz G C, Hersam M C and Duyne R P V 2017 *Chem. Rev.* **117** 4961
[26] Shao J and Su W 2022 *Nanoscale* **14** 17119
[27] Kumar N 2018 *Development of tip-enhanced Raman spectroscopy and its application to heterogeneous catalysis research* (Utrecht University)
[28] Huang T X, Cong X, Wu S S, Lin K Q, Yao X, He Y H, Wu J B, Bao Y F, Huang S C, Wang X, Tan P H and Ren B 2019 *Nat. Cimmun.* **10** 4455
[29] Lee C, Jeong B G, Yun S J, Lee Y H, Lee S M and Jeong M S 2018 *ACS Nano* **12** 9982
[30] Shao J, Chen F, Su W, Kumar N, Zeng Y, Wu L and Lu H W 2022 *J. Phys. Chem. Lett.* **13** 3304
[31] Su W, Kumar N, Shu H, Lancry O and Chaigneau M 2021 *J. Phys. Chem. C* **125** 26883
[32] Tang C, He Z, Chen W, Jia S, Lou J and Voronine D V 2018 *Phys. Rev. B* **98** 041402
[33] Yao Y, Chen F, Fu L, Ding S, Zhao S, Zhang Q, Su W, Ding X and Song K 2020 *J. Phys. Chem. C* **124** 7591
[34] Huang T X, Huang S C, Li M H, Zeng Z C, Wang X and Ren B 2015 *Analyt. Bioanalyt. Chem.* **407** 8177
[35] Sheng S, Wu J B, Cong X, Li W, Gou J, Zhong Q, Cheng P, Tan P H, Chen L and Wu K 2017 *Phys. Rev. Lett.* **119** 196803
[36] Yu W, Wang Z S, Zhao X X, Wang J Y, Herng T S, Ma T, Zhu Z Y, Ding J, Eda G, Pennycook S J, Feng Y P and Loh K P 2020 *Adv. Funct. Mater.* **30** 2003057
[37] Smithe K K H, Krayev A V, Bailey C S, Lee H R, Yalon E, Aslan Ö B, Muñoz Rojo M, Krylyuk S, Taheri P, Davydov A V, Heinz T F and Pop E 2018 *ACS Appl. Nano Mater.* **1** 572
[38] Ghoshal D, Yoshimura A, Gupta T, House A, Basu S, Chen Y W, Wang T M, Yang Y, Shou W J, Hachtel J A, Idrobo J C, Lu T M, Basuray S, Meunier V, Shi S F and Koratkar N 2018 *Adv. Funct. Mater.* **28** 1801286
[39] Lloyd D, Liu X H, Christopher J W, Cantley L, Wadehra A, Kim B L, Goldberg B B, Swan A K and Bunch J S 2019 *Nano Lett.* **19** 7548
[40] Guo Y, Li B, Huang Y, Du S, Sun C, Luo H L, Liu B L, Zhou X J, Yang J L, Li J J and Gu C Z 2020 *Nano Res.* **13** 2072
[41] Yagmurcukardes M, Bacaksiz C, Unsal E, Akbali B, Senger R T and Sahin H 2018 *Phys. Rev. B* **97** 115427
[42] Darlington T P, Krayev A, Venkatesh V, Saxena R, Kysar J W, Borys N J, Jariwala D and Schuck P J 2020 *J. Chem. Phys.* **153** 024702
[43] Long Y, Jiang Z, Gao Z, Li B, Li X, Liu X, Yin J and Guo W 2023 *Extreme Mech. Lett.* **60** 101978
[44] Liu E, Zhu B and Luo J eds 2008 *Semiconductor physics* (Beijing: Publishing House of Electronics Industry)
[45] Min Y M, Wang A Q, Ren X M, Liu L Z and Wu X L 2018 *Appl. Surf. Sci.* **427** 942
[46] Yu Z G, Cai Y and Zhang Y W 2015 *Sci. Rep.* **5** 13783
[47] Zhang S S, Mao N N, Zhang N, Wu J X, Tong L M and Zhang J 2017 *ACS Nano* **11** 10366
[48] Feng Y Q, Zhou W, Wang Y J, Zhou J, Liu E F, Fu Y J, Ni Z H, Wu X L, Yuan H T, Miao F, Wang B G, Wan X G and Xing D Y 2015 *Phys. Rev. B* **92** 054110
[49] Mohamed N B, Shinokita K, Wang X F, Lim H E, Tan D Z, Miyauchi Y and Matsuda K 2018 *Appl. Phys. Lett.* **113** 121112
[50] Ma L, Wang Y C and Zhao Y P 2022 *J. Electron. Mater.* **51** 3919
[51] Kawata S 2007 *Tip enhancement* (Oxford: Elsevier)
[52] Kumar N, Rae A and Roy D 2014 *Appl. Phys. Lett.* **104** 123106
[53] Ichimura T, Fujii S, Verma P, Yano T, Inouye Y and Kawata S 2009 *Phys. Rev. Lett.* **102** 186101
[54] Puretzky A A, Liang L, Li X, Xiao K, Sumpter B G, Meunier V and Geohegan D B 2016 *ACS Nano* **10** 2736
[55] Zabel J, Nair R R, Ott A, Georgiou T, Geim A K, Novoselov K S and Casiraghi C 2012 *Nano Lett.* **12** 617
[56] Beams R, Cançado L G, Jorio A, Vamivakas A N and Novotny L 2015 *Nanotechnology* **26** 175702
[57] Komaragiri U, Begley M R and Simmonds J G 2005 *J. Appl. Mech.* **72** 203
[58] Niehues I, Deilmann T, Kutrowska-Girzycka J, Taghizadeh A, Bryja L, Wurstbauer U, Bratschitsch R and Jadczak J 2022 *Phys. Rev. B* **105** 205432